Hydrodynamics and Gas Mixing in a Carbon Nanotube Agglomerate Fluidized Bed

Hao Yu, Qunfeng Zhang, Guangsheng Gu, Yao Wang, Guohua Luo, and Fei Wei
Key Laboratory of Green Reaction Engineering and Technology, Tsinghua University, Beijing 100084, P. R. China

DOI 10.1002/aic.11031
Published online November 2, 2006 in Wiley InterScience (www.interscience.wiley.com).

A typical nanoscale fiber material, carbon nanotubes (CNTs), was fluidized in a 280 mm inner diameter (ID) nano-agglomerate fluidized bed (NAFB). The solids distribution and gas mixing were measured by a self-developed conductance method and the hydrogen tracer technique. Typical nano-agglomerate fluidization characteristics, such as high bed expansion ratio and multi-staged agglomerate structure, were observed. Fluidization experiments over a wide gas velocity range showed that the CNT agglomerates have agglomerate-bubbling-fluidization (ABF) characteristics. Particulate fluidization can also be achieved in the range 0.017~0.038 m/s, showing they also have Geldart-A particle characteristics. A systematic comparison of the transition velocities, solids distributions, and gas mixing between the fluidizations of CNT agglomerates and Geldart-A particles was carried out. CNT NAFBs have more non-uniform solids concentration profiles near the wall, but more homogenous micro-flow structures than Geldart-A particles, which leads to good gas mixing. These unique hydrodynamics behaviors are attributed to the difference in the microstructure between the nano-agglomerates and ordinary particles.
AIChE J, 52: 4110–4123, 2006
Keywords: carbon nanotube, nano-agglomerate, fluidization, solids fraction, gas mixing

Introduction

Nanoparticles in the size range of 1 to 100 nm have a variety of industrial applications due to their unique physical and chemical properties. The fluidization of nanoparticles can provide continuous handling, good mixing, and gas-solid contact, and high mass and heat transfer efficiency, and is an attractive technology in the fields of drug manufacture,[1] nanoparticle modification,[2,3] preparation of nanomaterials,[4,5] and elutriation of fine and cohesive particles.[6] Thus, nanoparticle fluidization is one of the most significant issues in fluidization science and technology.

The Geldart classification of powders[7] implies that nanoparticles would be difficult to fluidize due to their strong interparticle forces. However, some studies have shown that fine particles with diameters less than 0.5 μm, such as SiO_2,[8,9] carbon fibers,[10] and CuO/Al_2O_3 aerogels,[11] can be fluidized in the form of agglomerates. The fluidization characteristics of a variety of nanoparticles have been summarized.[12] Fluidization can be achieved in a wide range of particle density and size, but the formation of multi-staged agglomerate structures is essential.[8] Two types of nanoparticle fluidization, termed agglomerate particulate and bubbling fluidization (APF and ABF),[13] have been reported. The fluidization behaviors of nanoparticles depend on their material, density, size, and surface properties. For instance, particles with strong interparticle forces, such as heavy metal particles,[14] tend to fluidize in the form of ABF. In APF, a surprisingly smooth and highly porous fluidization can often be achieved, which is extremely attractive to engineers due to their smoothness and uniformity.

Current address of H. Yu is School of Chemical and Energy Engineering, South China University of Technology, Guangzhou 510640, P. R. China.
Correspondence concerning this article should be addressed to F. Wei at weifei@flotu.org.

Thus, many works have focused on improving the fluidization quality by external force excitations, such as magnetic force,[15] sound wave,[16] and vibration.[17]

However, although the understanding of the nature of the fluidization of nanoparticles has been rapid, experimental results on the fluidization in regimes other than APF and ABF are scarce, despite the practical significance of a full regime classification. Furthermore, although information on solids distribution and gas mixing are obviously significant for design and scale-up, these detailed hydrodynamic behaviors in a nanoparticle fluidized bed are also rarely reported. CNTs[18] are a novel nano-fiber material with excellent physical and chemical properties. Recently, we achieved the production of multi-walled CNTs on a scale of kilograms per hour in an NAFB.[19] It was shown that the CNTs tend to form agglomerates with multi-staged agglomerate structures during reaction.[20] The mass production of CNTs provides the opportunity to investigate the hydrodynamics of CNTs and the fluidization of nanoparticles. In the present work, we report the fluidization characteristics, such as minimum fluidization velocity, hysteresis, and flow regime transitions, and hydrodynamic behaviors, such as solids distributions and gas mixing, of CNTs in a fluidized bed. The results are compared with those of traditional particles to understand some universal characteristics of nanoparticles, which will help the process engineering and handling of nanoparticles.

Experimental Methods

Materials and experimental setup

The CNT materials were synthesized by propylene decomposition on an $Fe/Mo/Al_2O_3$ catalyst in a fluidized bed. The details have been reported elsewhere.[20] The product contains only ~4% catalyst ash as characterized by thermalgravimetric analysis (TG, TA2000); thus, it can be taken that it is mainly CNTs. The as-prepared CNTs are black powders with a low packing density of 50 kg/m^3. The true density of the CNT agglomerates, $\rho_a = 61.1 kg/m^3$, measured by a Micromeritics 9310 porosimeter, was a little higher than the packing density. The sizes of CNT agglomerates range from several to 500 microns.[20]

As shown in Figure 1, a fluidized bed mockup of 280 mm I.D. and 2 m high was constructed of plexiglas to investigate the hydrodynamics of the CNT agglomerates. An expanding segment of 500 mm diameter and a cyclone separator outside the bed were used to reduce entrainment of the solids. The CNT powder was fluidized with air at room temperature and ambient pressure. The fluidization phenomena were observed in a wide range of gas velocity from minimum fluidization to 0.3 m/s, which covered all the fluidization regimes except for pneumatic transport. The gas velocities were determined and controlled by glass rotameters, and the height and pressure drop of the bed were measured by a ruler and a U-type manometer. To observe the fluidization of the CNTs directly, the CNTs were fluidized in a plexiglas two-dimensional bed 300 mm wide and 20 mm thick. A video camera was used to record the fluidization of the CNTs.

Measurement of solids fractions

The axial profiles of section-averaged solids fractions were obtained from the pressure drop profiles, which were measured by U-type micromanometers of the ethyl acetate-water binary system. The measuring taps were uniformly distributed along the bed at intervals of 100 mm, as shown in Figure 1. The pressure drop data were converted to average solids fractions by:

$$\overline{\varepsilon_s} = \frac{\dfrac{h}{\Delta H}(\rho_{H_2O} - \rho_f)}{\rho_a - \rho_f} \tag{1}$$

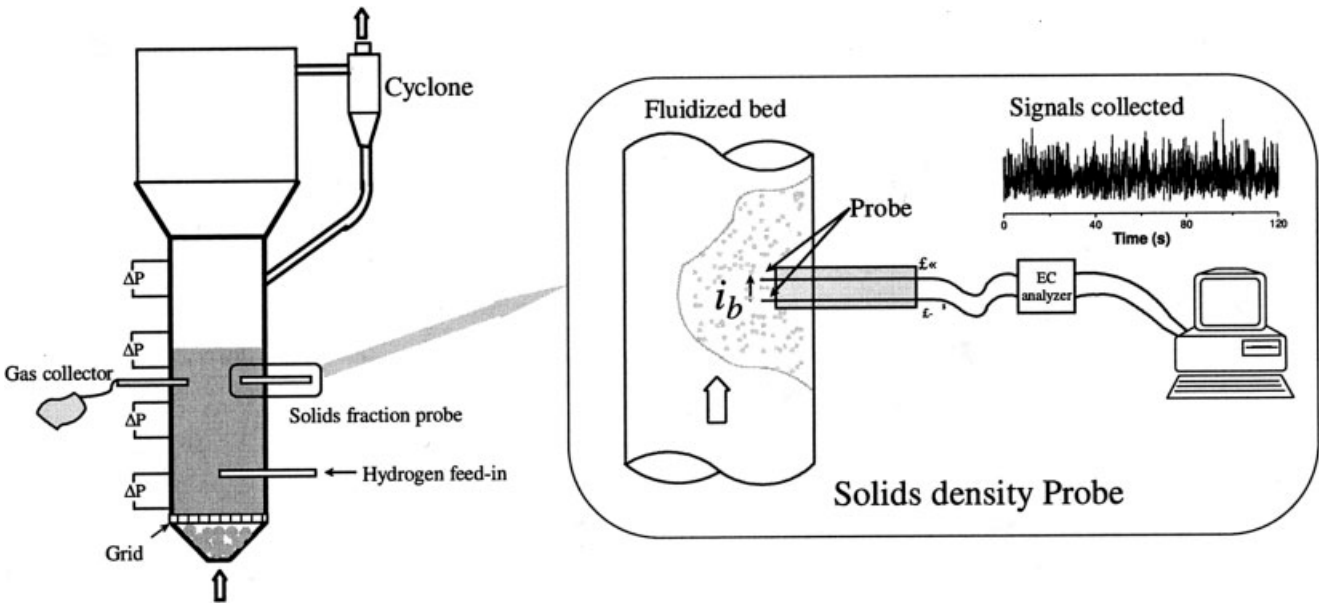

Figure 1. Experimental system.

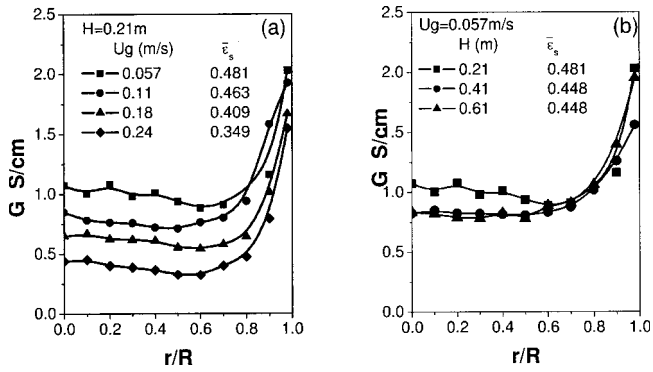

Figure 2. Distributions of conductance depending on (a) U_g and (b) H.

Since the CNTs are black powders and have extremely weak reflection to the incident light, it was difficult to use the conventional optical density probe method[21] to get good signals. In the present work, an electrical conductance method was developed to measure the local solids concentration in the CNT NAFB that is based on their conductance. The apparatus used in our experiments is schematically illustrated in the right part of Figure 1. It is well known that fluidized conductive particles can transfer charges by interparticle collision.[22,23] Thus, currents can be immerged between two conductive balls with differential potentials immersed in the fluidized conductive particles.[24,25] For spherical probing balls, monodispersed particles, and elastic collision, the dependence of the induced current on solids concentration has been derived as:[25]

$$i_b = A(d_p + d_b)^2 (V_{p0} - V_{b0}) n U_p^{(8/5)} \tag{2}$$

where A is a constant related to the system. Thus, the observed conductance can be considered a function of the solids concentration, particle velocity and diameter, and experimental dimensions that can be practically measured with a probe as shown in Figure 1, namely:

$$G = f(\varepsilon_s, U_p, d_p, \Delta V, L) \tag{3}$$

Figure 2 shows the variations of the radial distributions of the measured conductance with the superficial gas velocity and height. It indicates that the local conductance is strongly influenced by the local solids fraction. The particle velocity term is hard to determine in a dense fluidized bed, but it is related to the gas velocity and particle concentration. As an approximation, when the gas velocity is not high, we can neglect its contribution to G. An attempt to include a gas velocity term in the correlation, namely, $G = BU_g^{\alpha 1} (\varepsilon_s - \varepsilon_{s0})^{\alpha 2}$, was made, but no significant improvement in accuracy was obtained. Although the agglomerate sizes often decreased with increasing bed heights,[26] Figure 2b indicates that the variation is not much. In addition, CNTs are highly conductive and can be used as an anti-electrostatic material,[27] which allows a reasonable assumption of excluding the effect of electrostatic charges. Thus, with fixed ΔV and L, we can use a power function to describe the relationship between the observed conductance and solids fraction:

$$G = B(\varepsilon_s - \varepsilon_{s0})^{\alpha} \tag{4}$$

A transformation of Eq. 4 gives the following equation:

$$\varepsilon_s = CG^{\beta} + \varepsilon_{s0} \tag{5}$$

By measuring the section-averaged solids fractions, the constants in Eq. 5 were obtained by regression as: $C = 8.01$, $\beta = 0.664$, and $\varepsilon_{s0} = 0.0580$.

By sampling the current i_b at a frequency of 16.7 Hz for 2 min, the time-averaged conductance can be obtained. Using the above correlation, the maximum error was 15% and the average error was less than 5% for the conditions we investigated. Using the above validated correlation, one can convert a measured time-dependent conductance sequence into a series of transient solids fraction signals,[28] and analyze the micro-structure of the gas-CNT flows.

Measurement of axial and radial gas dispersion coefficients

A steady-state hydrogen tracer technique[29] was used to obtain the axial and radial gas dispersion coefficients in the CNT NAFB. The experimental technique is also illustrated in Figure 1. The tracer was continuously injected into the center of the bed, 0.3 m above the gas distributor, at a flow rate approximately equal to 1/1000 of the fluidizing gas flow rate, and collected by a gas collector 100 mm downstream of the injection, as shown in Figure 1. The tracer concentrations were detected by a TCD detector immediately. A two-dimensional dispersion model (see ref. 30 for model details) gives:

$$\frac{\partial^2 \Gamma}{\partial \xi^2} + \frac{1}{\sigma}\frac{\partial}{\partial \sigma}\left(\sigma \frac{\partial \Gamma}{\partial \sigma}\right) = 2\varphi \frac{\partial \Gamma}{\partial \xi} \tag{6}$$

with boundary conditions:

$$\begin{cases} \sigma = 0 & \dfrac{\partial \Gamma}{\partial \sigma} = 0 \\ \sigma = 1 & \dfrac{\partial \Gamma}{\partial \sigma} = 0, \\ \sigma = -\infty & \Gamma = 0 \end{cases}$$

where $\rho = \frac{r}{R}$, $\xi = \frac{D_r^{(1/2)} Z}{D_a^{(1/2)} R}$, $\varphi = \frac{U_g R}{2 D_a^{(1/2)} D_r^{(1/2)}}$, and $\Gamma = \frac{C}{C_0}$. Its analytical solution[31] is:

$$\Gamma = \varphi \sum_{n=0}^{\infty} \frac{J_0(\sigma K_n) \exp\left[-\xi \cdot \left(-\varphi + \sqrt{\varphi^2 + K_n^2}\right)\right]}{J_0^2(K_n)\sqrt{\varphi^2 + K_n^2}} \qquad \xi \geq 0 \tag{7}$$

$$\Gamma = \varphi \sum_{n=0}^{\infty} \frac{J_0(\sigma K_n) \exp\left[\xi \cdot \left(\varphi + \sqrt{\varphi^2 + K_n^2}\right)\right]}{J_0^2(K_n)\sqrt{\varphi^2 + K_n^2}} \qquad \xi \leq 0 \tag{8}$$

where J_n is the nth order Bessel function, and K_n the nth positive solution of the equation $J_1(K_n) = 0$. By measuring the concentration profiles, the axial and radial dispersion coefficients can be extracted. Figure 3 shows the agreement between the prediction of the steady state hydrogen concentration distributions with experimental data at different gas velocities.

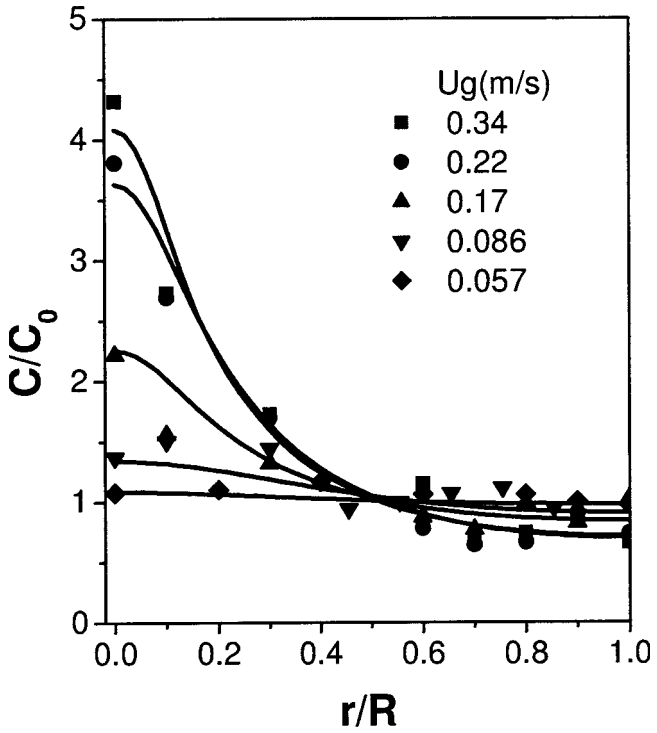

Figure 3. Profiles of tracer concentrations.

Results and Discussion

Fluidization characteristics of a CNT agglomerate fluidized bed

A bed expansion experiment was carried out in a CNT fluidized bed with 345 mm static bed height. The bed expansion was repeatedly measured several times using a sufficiently long equilibrium time (~10min for each experimental point) to get reliable results. Figure 4 shows the expansion behavior of the CNT fluidized bed and typical images in the various regimes. As the gas velocity increased, gas channeling first appeared in the bed and the upper interface of the bed fluctuated violently (see Figure 4a), along with a fluctuation of the pressure drops. When U_g was larger than 0.06 m/s, the materials were apparently fluidized (see Figure 4b). However, the rapid increase in the pressure drop indicated that CNTs were not fully suspended and did not form stable agglomerates in this regime. From 0.06 m/s to 0.1 m/s, the bed height increased rapidly and expanded two-fold. When U_g was above 0.1 m/s, the bed expansion slowed down and the pressure drop remained stable, indicating the formation of fully suspended agglomerates. Bubble break-up dominated the fluidization, no obvious bubbles could be observed, and the interface of the bed was blurred due to the ejection of particles into the free space (see Figure 4c). When U_g was higher than 0.2 m/s, the bed expanded to 3.5 times its initial height, and serious entrainment occurred as the bed was operated in fast fluidization. Different height/pressure drop-velocity dependences were recorded with decreasing gas velocity from 0.2 m/s to defluidization. A stable ABF can be maintained to 0.038 m/s in the defluidization branch, with slightly changed pressure drops. Below 0.038 m/s, there was smooth particulate fluidization (see Figure 4d). This particulate fluidization can be maintained in the range of 0.017–0.038 m/s, and the bed height decreased with deceasing gas velocity. When the gas velocity was lower than 0.017 m/s, channeling appeared again and the bed defluidized (see Figure 4e). Taking into account the fact that the CNTs were fluidized with bubbles under most of the conditions, we can consider CNTs as ABF particles, although particulate fluidization also exists.

Generally, the fluidization hysteresis can be attributed to the contact stresses and wall friction and is dependent on the scale of the bed.[32] In the present work, the role of wall friction can be neglected due to the large diameter of the experimental set-up, and the contact stress dominates the initial fluidization. For nanoparticle fluidizations, a strong hysteresis phenomenon has been found with different materials, such as goethite,[12] talcum powder,[12] and SiO_2.[13] The reason is that different energies are required for the initial fluidization of the beds and suspending the fluidizing agglomerates. The inter-particle forces between the fluidized agglomerates are weaker than that of contacting nanoparticles in packed beds. The huge area enclosed in the fluidization and defluidization branches indicates the significant reduction of the inter-particle forces between the agglomerates after the formation of the CNT agglomerates, which is due to their complex surface structure and entangled chain-like network, and demonstrates that the macroscopic flow behaviors can be closely related to the microstructure in nanoparticle systems. Due to the serious hysteresis in CNT agglomerate fluidization, the reproducibility is poor and the particulate fluidization regime cannot be observed in the fluidization branch. Thus, only data from the defluidization branch is used to determine the fluidization parameters in the following text.

As described earlier, although CNT agglomerates were mainly fluidized with bubbles, they also exhibited characteristics of Geldart-A particles and can be particulately fluidized. It was observed that the minimum fluidization and bubbling velocities were about 0.017 m/s and 0.038 m/s. Since particulate fluidization existed in the CNT fluidized bed, the Richardson-Zaki equation can be used to obtain the terminal velocity and agglomerate size, based on which the minimum fluidization velocity can be calculated.[8] The mass balance of powder in bed gives:

$$\varepsilon = 1 - \frac{H_0}{H} \cdot \frac{\rho_b}{\rho_a}. \tag{9}$$

As shown in Figure 5, the particulate fluidization of the CNT agglomerates agrees well with the R-Z equation, by which the terminal velocity of the CNT agglomerates was determined as 0.205 m/s. Zhu et al[9] have verified that the highly porous nano-agglomerates can be treated as solid particles for the hydrodynamics analysis. For $Re_t > 2$, the agglomerate size can be calculated from the Allen equation:

$$d_a = 1.23 \frac{U_t^{0.875} \rho_f^{0.25} \mu_f^{0.375}}{(\rho_a - \rho_f)^{0.625}}, \tag{10}$$

where air properties at 101.33 kPa and 20°C are used:

$$\rho_f = 1.205 \text{ kg m}^{-3} \text{ and } \mu_f = 1.81 \times 10^{-5} \text{ Pa} \cdot \text{s}.$$

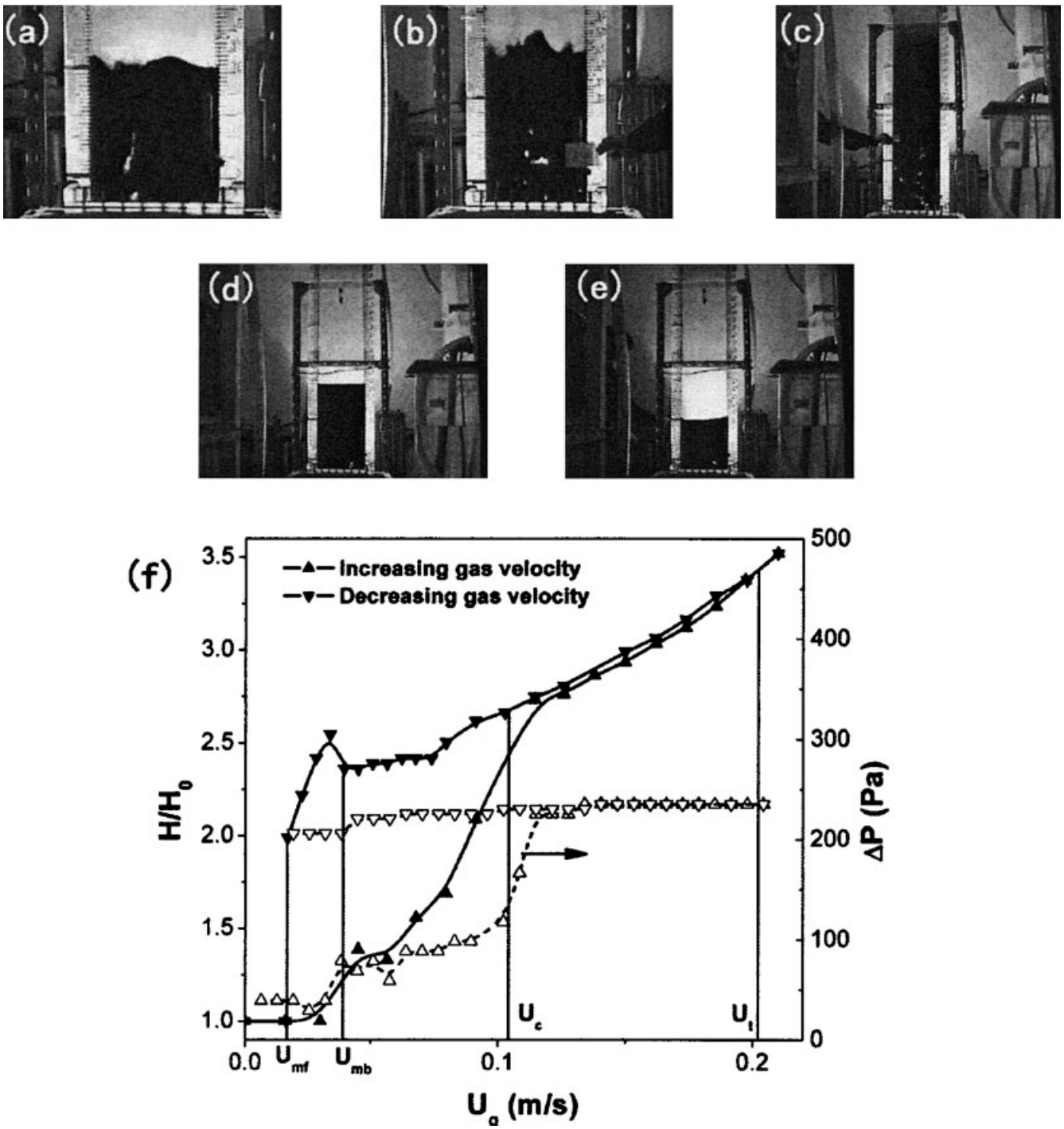

Figure 4. Dependences of bed expansion and pressure drop on gas velocity of a CNT NAFB (f).

The fluidization in the various regimes was recorded with a 2-D bed and illustrated for (a) channeling, (b) ABF, (c) turbulent, (d) particulate, and (e) defluidization.

Thus, the agglomerate size $d_a = 416\mu$m can be calculated. With these agglomerate properties, the minimum fluidization, transition,[33] and serious entrainment velocity[34] can be estimated and compared with Geldart-A particles. These are listed in Table1.

Serious entrainment takes place at $U_g > 0.2$, which agrees well with the calculated terminal velocity. This allows us to draw the conclusion that fast fluidization occurs when $U_g >$ 0.2 m/s. However, errors will arise in the values of the other parameters from the assumption that a nano-agglomerate is a Geldart-A single particle. The calculated minimum fluidization velocity is slightly higher than the observed velocity, while the calculated U_c and U_{se} are much higher than the observed values. The too-high estimate of U_c and U_{se} indicates that the

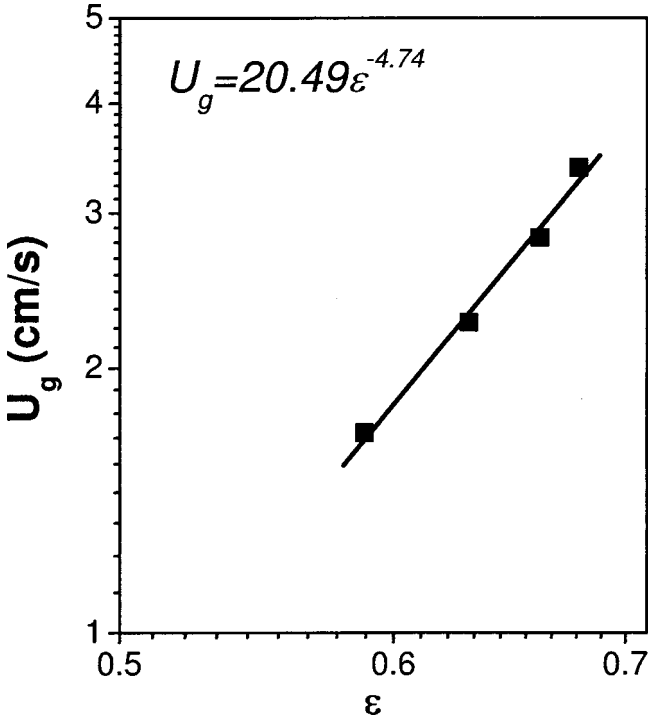

Figure 5. Logarithmic plot of the bed voidage vs. the superficial gas velocity.

weak interaction among the CNT agglomerates and the highly porous structure increased the overall voidage and reduced the drag coefficient for the agglomerates, which reduced U_c and U_{se} and made U_{se} approach U_t. The above comparison confirms and emphasizes the uniqueness of the fluidization of nanoparticles, and more detailed case studies are essential for the accumulation of knowledge on their fluidization.

Solids distributions in a CNT agglomerate fluidized bed

Axial Profiles of Section-Averaged Solids Fractions. The axial profiles of section-averaged solids fractions of particulate fluidization, ABF, and turbulent regimes were measured and plotted in Figure 6. In the particulate fluidization regime, the solids were distributed uniformly along the bed height. In the ABF regime, the voidage increased and an ejection space appeared on the fluidizing bed. When operating in the turbulent regime, a typical S type solids distribution was observed. Generally, the axial distribution characteristics of the CNT agglomerates are similar to conventional particle fluidization.

Equation 5 means that a critical solids fraction exists below which the gas-CNT flow is too dilute to construct a conductive network, where G cannot be measured. Equation 5 is in the form of a percolation law with a percolation threshold of 0.0580 and a percolation index of 1.51. Since the threshold distinguishes the dense and dilute phases, it can be used as a criterion for the ejection space in a turbulent fluidized bed. As shown in Figure 6, this criterion ($\varepsilon_{s0} = 0.0580$) agrees well with experimental data, validating the conductance method used in the present work.

Radial Solids Fraction Distributions in the Particulate Fluidization Regime. The radial solids fraction profiles in particulate and aggregative fluidization were investigated. Figure 7 shows the radial distributions of solids fractions in a CNT NAFB and their variation with U_g in the particulate fluidization regime. The solids were uniform when U_g was relatively high. However, the distribution gradually became nonuniform near the wall with decreasing U_g and increasing solids fractions. Near U_{mf}, the much higher solids concentration near the wall led to a typical "core-annulus" flow structure. The changes in the solids distribution are also helpful for an understanding of the defluidization of CNTs. As the CNT NAFB defluidized, the solids near the wall first aggregate due to the wall friction. During the collapsing of the CNT particulate fluidization, the collapsed bed volume is mainly redistributed into the annulus area, leading to the increase of the solids concentration near the wall. If the annulus is dense enough, the bed will be unstable and fully defluidized. This insight into the flow structure of particulate fluidization reveals the non-uniformity contained in the apparent uniform expansion.

Radial Solids Fraction Distribution in the Aggregative Fluidization Regimes. In the aggregative fluidization regimes

Table 1. Fluidization Parameters of the CNT Agglomerates

	d_a (μm)	ρ_a (kg/m^3)	U_{mf} (m/s)	U_{mb} (m/s)	U_c (m/s)	U_t (m/s)	U_{se} (m/s)
Observed	416[a]	61.1	0.017	0.038	~0.1	0.205	>0.2
Calculated	–	–	0.020[b]	–	0.330[c]	–	0.69[d]

[a]by

$$d_a = 1.23\ \frac{U_t^{0.875}\rho_f^{0.25}\mu_f^{0.375}}{(\rho_a-\rho_f)^{0.625}}$$

[b]by

$$U_{mf} = \frac{(\phi_s d_p)^2}{150}\frac{(\rho_p-\rho_f)g}{\mu_f}\left(\frac{\varepsilon_{mf}^3}{1-\varepsilon_{mf}}\right)$$

[c]by Cai's criterion[33]

$$\frac{U_c}{\sqrt{gd_p}} = \left(\frac{\mu_{f0}}{\mu_f}\right)^{0.2}\left[K\left(\frac{\rho_{f0}}{\rho_f}\right)\left(\frac{\rho_p-\rho_f}{\rho_f}\right)\left(\frac{D}{d_p}\right)\right]^{0.27}$$

$$K = \left(\frac{0.211}{D^{0.27}} + \frac{2.42\times10^{-3}}{D^{1.27}}\right)^{(1/0.27)}$$

[d]by

$\mathrm{Re}_{se} = 1.53\ Ar^{0.50}$ (see ref. 34)

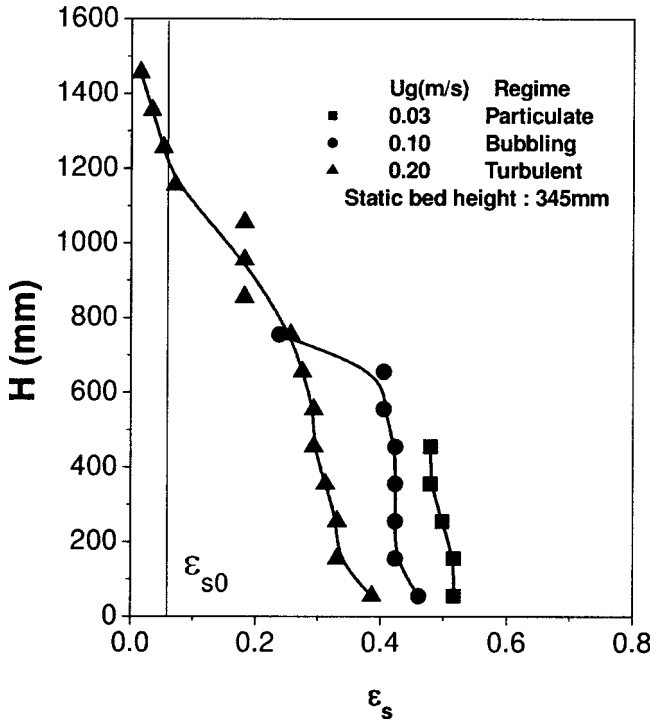

Figure 6. Axial profiles of the solids fractions in a CNT NAFB.

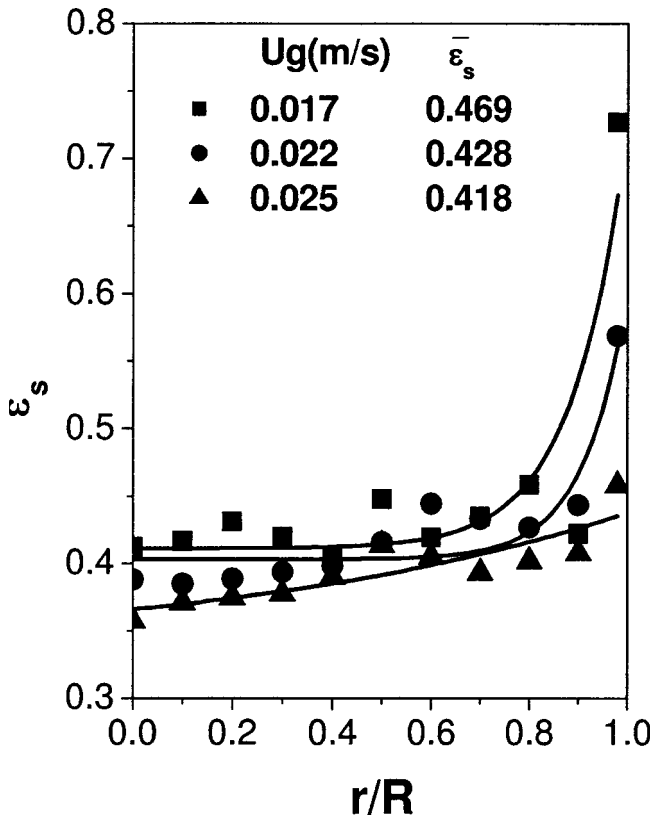

Figure 7. Radial solids fraction profiles in particulate fluidization of a CNT NAFB.

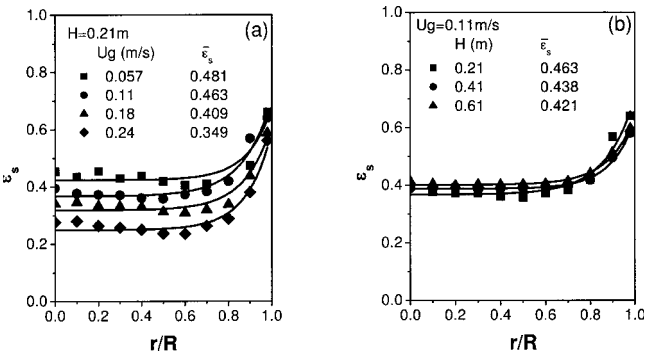

Figure 8. Variations of solids fractions with (a) the superficial gas velocity and (b) bed height.

(bubbling and turbulent regimes), the radial solids fraction was almost constant at the center of the bed, but increased when the relative radii were larger than 0.8. The maximum was reached at the wall. As shown in Figure 8, the solids profiles vary with both U_g and H, but the stronger influence of U_g on the solids concentration makes the profiles vary more with U_g. Wang[35] has proposed that the solids profile in a FCC fluidized bed can be normalized and expressed by:

$$\frac{\varepsilon_s}{\bar{\varepsilon}_s} = E + F\left(\frac{r}{R}\right)^{\chi}. \tag{11}$$

The above equation can also be adopted for CNT agglomerate fluidization by taking into account the strong dependence of solids fractions on the section-averaged solids concentrations. The normalization requires:

$$\int_0^t 2 \cdot \left(\frac{r}{R}\right) \cdot \frac{\varepsilon_s}{\bar{\varepsilon}_s} \cdot d\left(\frac{r}{R}\right) = 1. \tag{12}$$

Equations 11 and 12 give:

$$F = \frac{\chi + 2}{2}(1 - E). \tag{13}$$

So, Eq. 11 can be transformed to:

$$\frac{\varepsilon_s}{\bar{\varepsilon}_s} - \frac{\chi + 2}{2}\left(\frac{r}{R}\right)^{\chi} = E\left[1 - \frac{\chi + 2}{2}\left(\frac{r}{R}\right)^{\chi}\right]. \tag{14}$$

By a linear fit to the

$$\left[\frac{\varepsilon_s}{\bar{\varepsilon}_s} - \frac{\chi + 2}{2}\left(\frac{r}{R}\right)^{\chi}\right] - \left[1 - \frac{\chi + 2}{2}\left(\frac{r}{R}\right)^{\chi}\right]$$

plot, E and F were determined. Table 2 shows the parameters obtained by assuming different χ. An acceptable precision was

Table 2. Comparison of Models Used to Calculate the Local Solids Fraction

	E	F	R
$\gamma = 6$	0.849	0.604	0.996
$\gamma = 7$	0.860	0.630	0.997
$\gamma = 8$	0.870	0.652	0.997

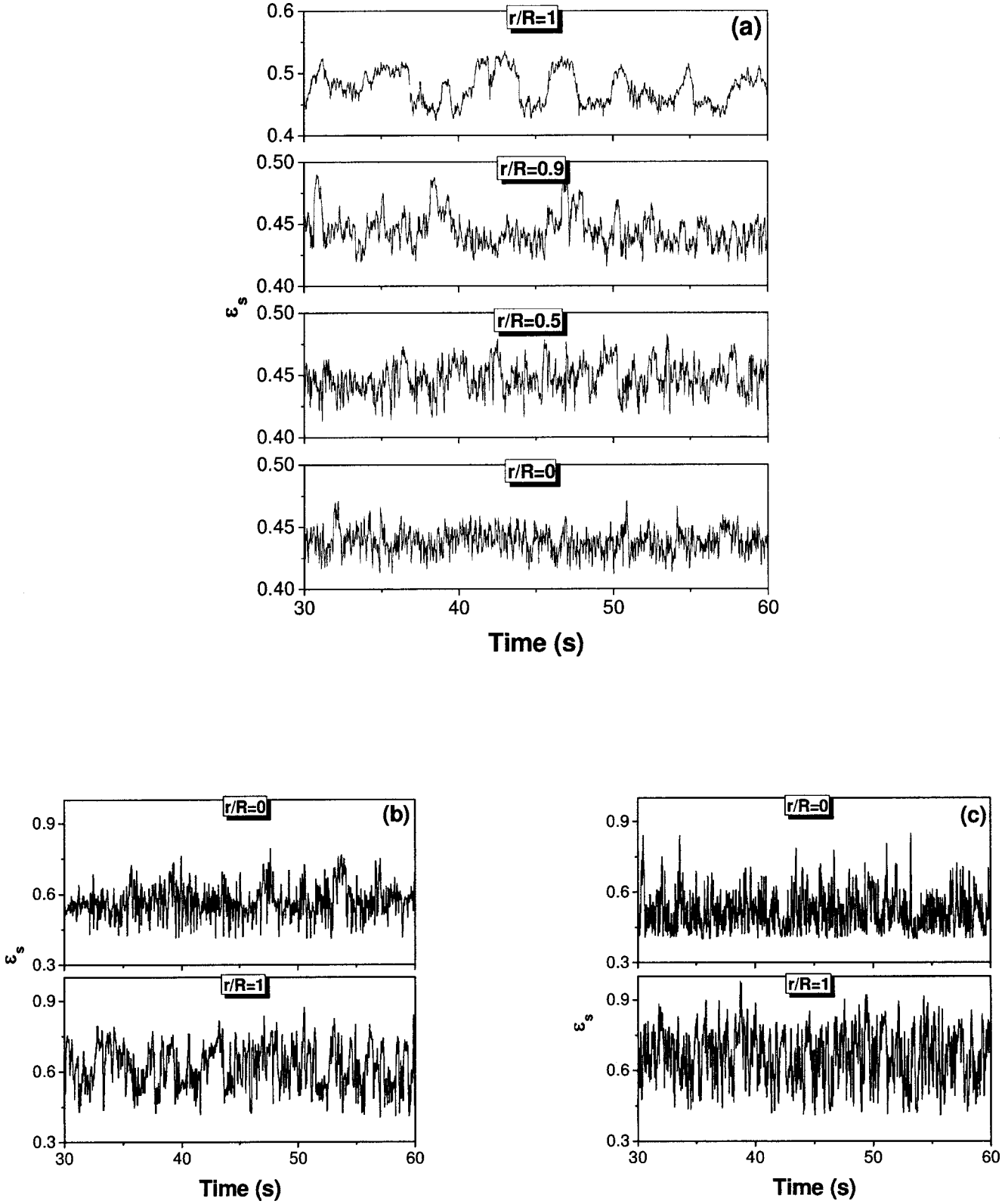

Figure 9. The transient density signals in (a) particulate fluidization (U_g = 0.028 m/s), (b) ABF (U_g = 0.057 m/s), and (c) turbulent fluidization (U_g = 0.18 m/s).

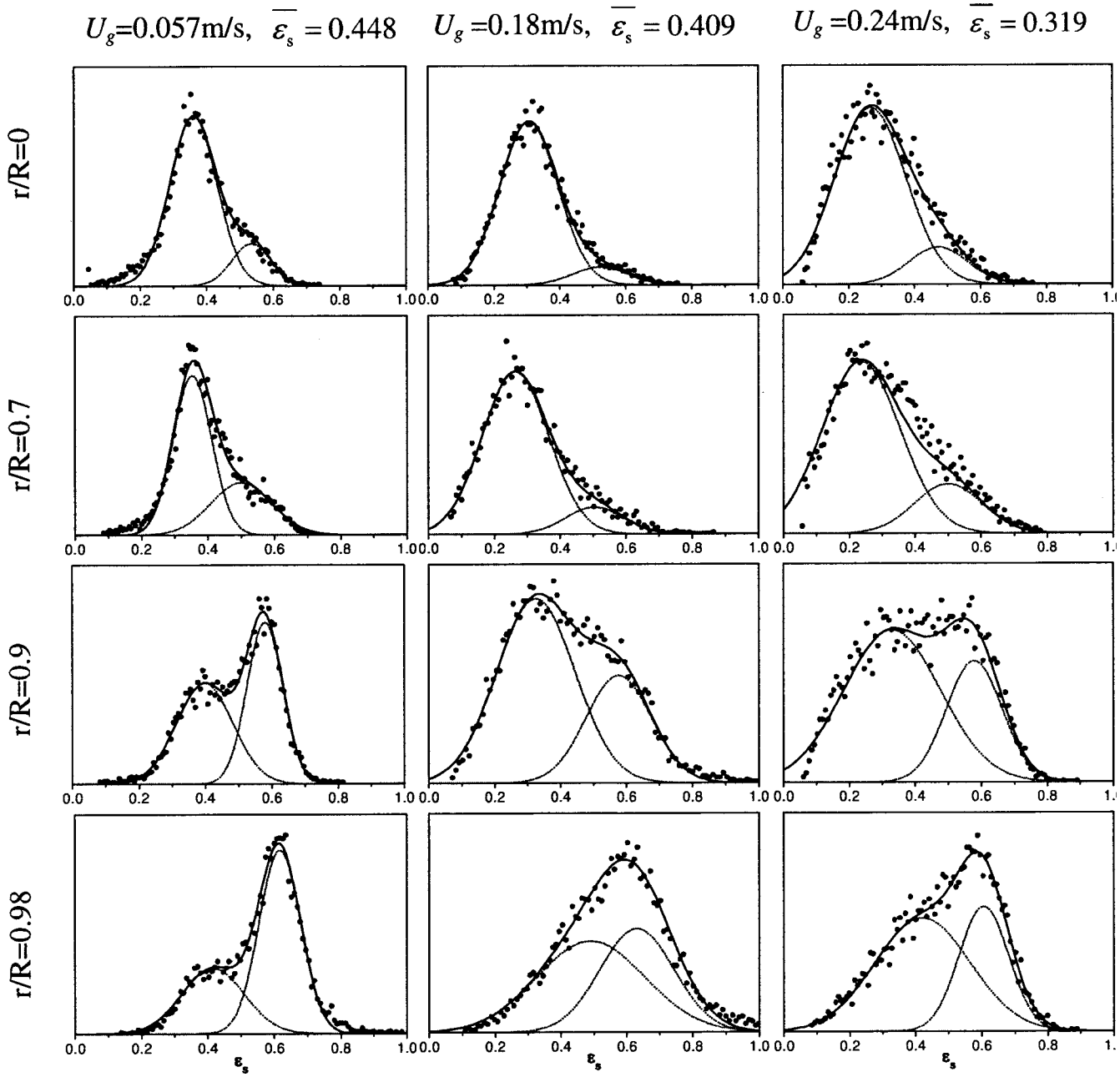

Figure 10. PDDs of transient densities in a CNT NAFB.

obtained at $\chi = 7$, and the local solids fraction in the aggregative fluidization can be calculated by:

$$\frac{\varepsilon_s}{\overline{\varepsilon_s}} = 0.860 + 0.630 \cdot \left(\frac{r}{R}\right)^7. \tag{15}$$

In the fitting procedure, the distribution for $U_g = 0.24$ m/s was also included, although the gas velocity was higher than the significant entrainment velocity. This velocity is very close to the significant entrainment velocity 0.2 m/s, which gave a higher solids fractions than that reported for Group A particles in fast fluidization (commonly less than 0.2 but operated under the much higher velocity than the significant entrainment velocity) and allowed a self-consistent fitting. Compared to Geldart-A particles, the solids radial distribution in a CNT NAFB is similar but more non-uniform near the wall ($\chi = 4$ for FCC[35]). This is probably caused by the stronger interactions among the nano-agglomerates due to wall friction and low gas shear force than is the case with conventional fine particles, which result in the aggregation of nano-agglomerates near the wall.

Transient Density Signal Analysis and Two-Phase Micro-Structure Flow in Gas-CNT Fluidization. Figure 9 shows typical transient densities in particulate fluidization, ABF, and turbulent fluidization. In particulate fluidization, the characteristics of the transient density were strongly dependent

on the radius. The fluctuation frequency of density signals was much higher at the center than near the wall. At r/R = 1, the wave crests and troughs, representing dense and dilute phases, respectively, were at intervals of several seconds, that is, there was the characteristic of creeping flow in this regime. The slow solid renewal near the wall clearly indicated much aggregation of nano-agglomerates, in agreement with the conclusion drawn from the analysis of time-averaged solids concentrations. It should be noted that the particulate fluidization may have nonuniform solids profiles and micro flow structures, despite its apparent uniformity.

In aggregative (bubbling and turbulent) fluidization, random fluctuating signals can be seen in the transient density time series. However, the signals are mainly at the values of about 0.6 and 0.4 near the wall, indicating that a two-phase flow structure existed at these locations. Generally, the two phases refer to the bubbles and emulsion phase in ABF, and voidage and clusters in turbulent and fast fluidizations.[28,36] In the following text, we do not distinguish these but denote them as dilute and dense phases. In order to extract the characteristics of the micro-structure in a CNT NAFB, a statistical analysis on the transient density signals was carried out. Figure 10 shows a typical probability density distributions (PDD) of the transient density signals at different U_g and radii. In aggregative fluidization, clear bimodal PDDs were obtained, which is like that of traditional particles.[28] As shown in Figure 10, the flow was dominated by the dilute phase at the center of bed, whereas the dense phase dominates the flow at r/R $>$ 0.7, indicating the tendency towards aggregation of nano-agglomerates near the wall.

As shown in Figure 10, the PDDs in the present work can be well described by a combined probability distribution of two normal probability density functions as:

$$p(\varepsilon_s) = \frac{1-\phi}{\sqrt{2\pi}\sigma_1} e^{((\varepsilon_s-\varepsilon_{s1})^2)/(2\sigma_1^2)} + \frac{\phi}{\sqrt{2\pi}\sigma_2} e^{((\varepsilon_s-\varepsilon_{s2})^2)/(2\sigma_2^2)} \quad (16)$$

By nonlinear fitting to the experimental data of the transient density with Eq. 16, the solids fraction of the dense and dilute phases (ε_{s1} and ε_{s2}), and the dense phase volume fraction ϕ can be obtained. Figure 11 shows the solids fraction distributions of the dense and dilute phases at different U_g. ε_{s1} and ε_{s2} decreased a little with increasing U_g. At a fixed U_g, the radial distributions of ε_{s1} and ε_{s2} were quite uniform except for a slight increase near the wall. The above results indicate that the micro-structures of the two phases are quite stable. Even though the two phases appear in both conventional and nanoparticle fluidizations, the micro-structures are different from each other. With fluid catalytic cracking (FCC) particles,[28] the solids fractions of the dilute phase are usually lower than 0.1, and the solids fractions of the dense phase are about 0.7, for values at their minimum fluidization. However, in the CNT agglomerate fluidization, although the dense phase also had about 60% solids close to the minimum fluidization, there were much higher solids fractions of about 0.3 in the dilute phase. Thus, the PDDs of the two phases in CNT agglomerate fluidization usually partly overlap each other, especially at high U_g and low average solids fraction. The above results indicate that a large amount of solids tend to enter the bubbles or voidages in a CNT fluidized bed. Thus, even though the radial profiles are more non-uniform than that of conventional particle fluidization, the non-uniformity is compensated by the more homogenous micro-flow structures in an NAFB, with significant benefits for the trans-

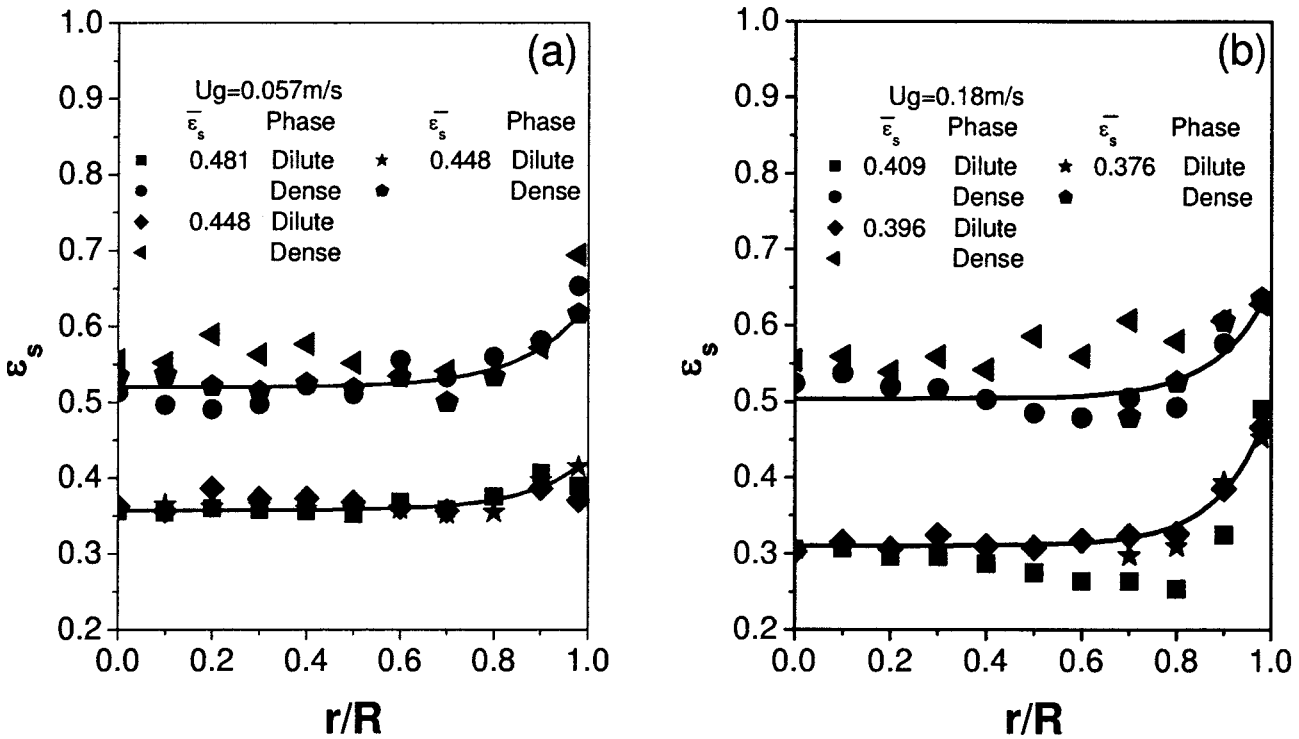

Figure 11. The solids fractions of the dense and dilute phases at (a) U_g = 0.057m/s and (b) 0.18m/s.

fer and mixing behaviors. It can be speculated that the homogenous micro-structure is caused by the highly porous structure of the nano-agglomerate and the high bed expansion ratio, which reduce the density difference between the gas and solids. Thus, solids can be easily transported into the bubbles or voidages, and the bubbles and voidages also tend to be dispersed in the emulsion phase. This is supported by observation on a 2-D fluidized bed. Shown in Figure 12 is an image of fluidized CNT agglomerates operating in the ABF regime that shows CNTs entering into bubbles, which makes the bubbles blurred.

Figure 13 shows the volume fractions of the dense phase ϕ in the different regimes. In ABF and turbulent fluidization, the dense phase maintained a constant volume fraction in the center of bed, but the volume fraction began to increase at r/R $>$ 0.6 and a maximum was reached at the wall. Strong radial non-uniformity can be seen in these regimes across the cross-section of the beds. However, a relatively uniform distribution of the dense phase volume fractions can be obtained in the fast fluidization regime because of a more homogenous micro-structure at high gas velocity.

As shown in Figure 14, the distributions of the phase volume fractions are similar at specific U_g in ABF and turbulent fluidization. The only exception is the condition U_g = 0.057m/s and H = 0.21 m, where ϕ is abnormally high at the center. This may have been caused by an experimental deviation because the micro-flow structure is dominated by the dense phase, which resulted in an ambiguous peak splitting. The two phases are also hard to distinguish when the dilute phase dominates the flow. Thus, it is only near the wall that the two phases exist under the operation conditions of U_g = 0.18 m/s and H = 0.61 m, as shown in Figure 14b. Nevertheless, the generally consistent distribution of ϕ implies that a quantitative description by a function of U_g and r/R is reasonable. Empirically, the following equation can be used to estimate the phase volume fractions in ABF and turbulent fluidization:

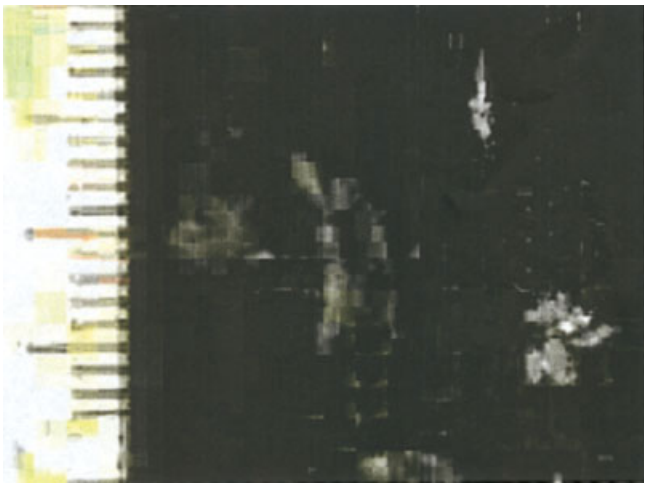

Figure 12. An image of the bubbles in a 2-D fluidized bed operating in the ABF regime.

[Color figure can be viewed in the online issue, which is available at www.interscience.wiley.com.]

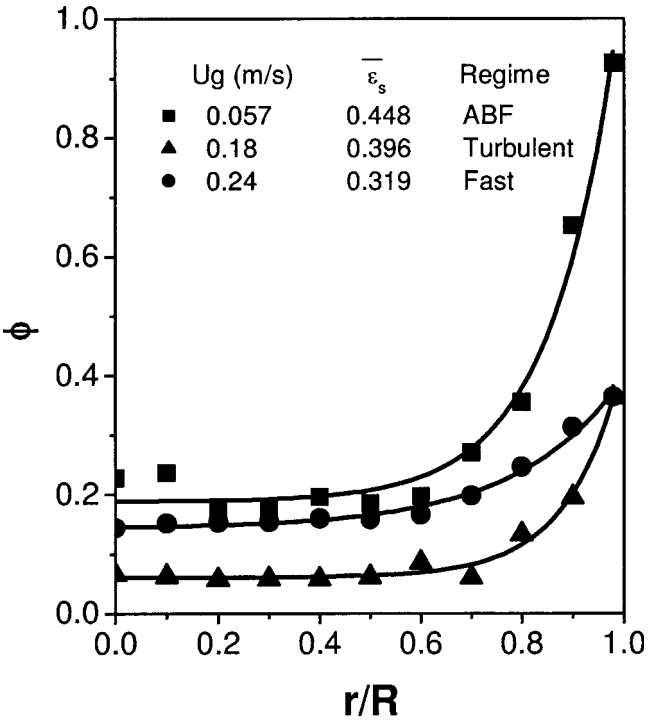

Figure 13. Volume fractions of the dense phase in the different regimes.

$$\phi = 0.632\left(\frac{U_g}{U_{mf}}\right)^{-0.928} + 0.512\left(\frac{r}{R}\right)^{6.29} \qquad (17)$$

in which the constants should be obtained by nonlinear regression. The solid lines in Figure 14 show the accuracy of Eq. 17, with less than 50% relative errors within the conditions in the present work. It should be noted that Eq. 17 has a form similar to Eq. 15, indicating that the phase volume fraction plays a quite significant role in determining the solids fraction distributions. By the above results, it can be concluded that the increase in solids fraction near the wall is mainly caused by the aggregation of nano-agglomerates.

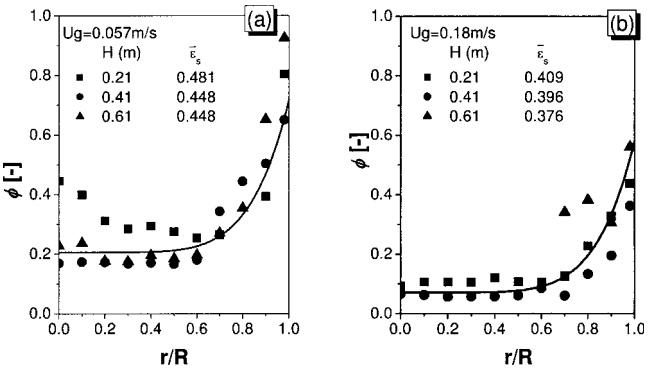

Figure 14. Distributions of the volume fractions of the dense phase in (a) ABF and (b) turbulent fluidization.

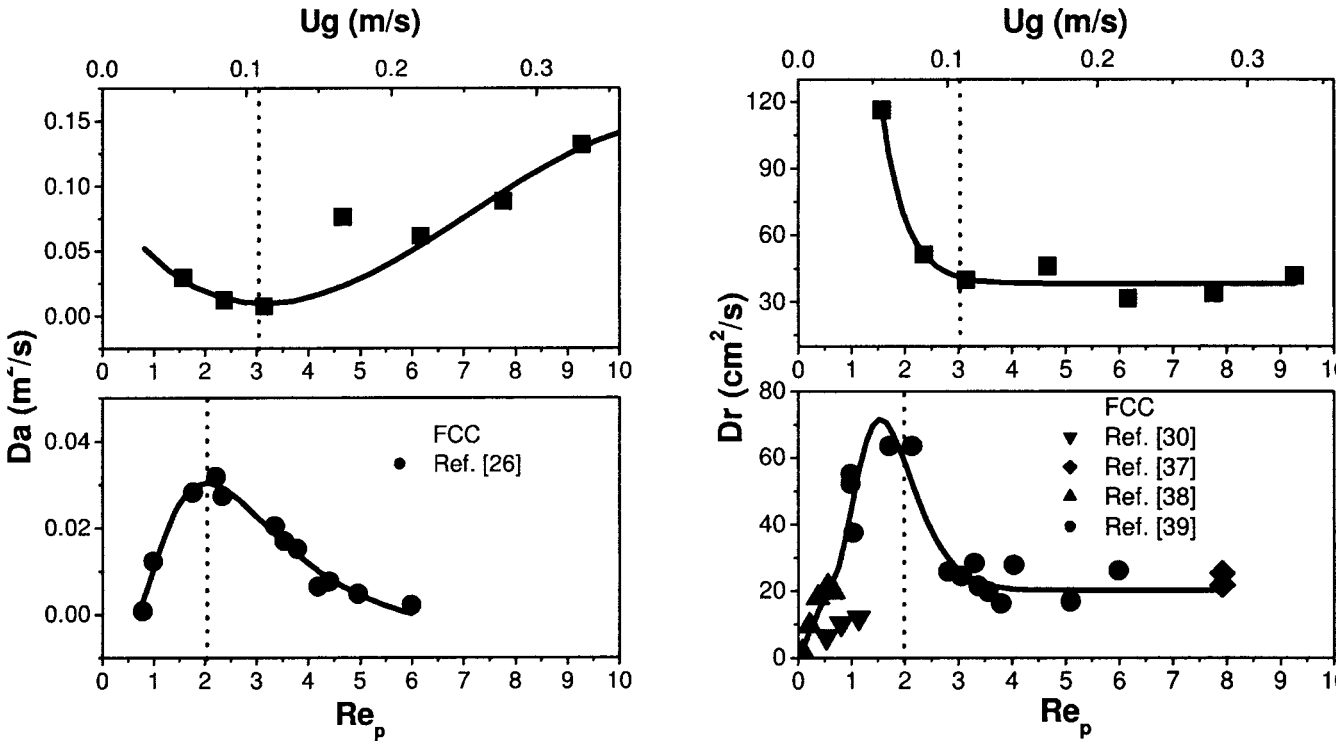

Figure 15. Comparison of the gas dispersion coefficients of CNT and FCC fluidized beds.

Gas mixing in a CNT agglomerate fluidized bed

A preliminary study on the gas mixing behavior in a CNT NAFB was conducted. Figure 15 compares the axial and radial gas dispersion coefficients of the CNT agglomerates and FCC particles.[30,37–39] Despite the huge differences between the properties of the nano-agglomerates and FCC particles, the CNT NAFB has gas dispersion coefficients on the same order of a FCC fluidized bed, namely about 10^1 m^2/s for D_a and 10^2 cm^2/s for D_r. Since the CNT NAFB was operated at far lower gas velocities, the $\mathrm{Re_p}$-D plots ($\mathrm{Re}_p = U_g d_p \rho_f / \mu_f$) were used to evaluate their gas mixing behaviors. For FCC particles, a maximum dispersion coefficient exists at $\mathrm{Re_p} = 2$. In contrast, D_a of the CNTs has a minimum at $\mathrm{Re_p} = 3$. For $\mathrm{Re_p} < 3$, both D_a and D_r of the CNTs decreased with increasing U_g. For $Re_p > 3$, D_a of the CNTs increased and D_r leveled off. Compared to the FCC particles, higher dispersion coefficients were obtained at a low gas velocity. Although the reason for the sharp decrease in the dispersion coefficients in the turbulent regime of FCC particles is controversial, a transition from bubbling to turbulent fluidization can be reflected by the maxima in the dispersion coefficients.[30] Analogously, we propose that such an extremum in CNT fluidization can also define U_c. Using this criterion, the transition velocity from bubbling to turbulent fluidization is roughly determined by $Re_p = 3$, namely, $U_g = 0.11$ m/s, which agrees with the observed data.

As shown in Figure 15, a different trend of dispersion coefficients against $\mathrm{Re_p}$ from that of Geldart-A particles was experimentally obtained. It is possible that the difference results from the network structure of the CNT agglomerates, which can act to increase the roughness of the agglomerates and benefit gas mixing at low gas velocities. At high gas velocities, it has been predicted that a homogenous microstructure will enhance gas mixing. The gas becomes almost continuous and dominates the gas mixing in a CNT NAFB operating at high U_g, leading to the increase of D_a. However, the relationship between gas mixing and the nature of the fluidized nano-agglomerates is not yet fully understood and more detailed work is needed.

Conclusions

Fluidization characteristics, solids distributions, and gas mixing behaviors were investigated in a CNT NAFB. A smooth and highly expanded fluidization was achieved, but a strong hysteresis exists in the CNT fluidization. On the defluidization branch, similar to Geldart-A particles, particulate fluidization, ABF, turbulent, and fast fluidizations can be successively observed and distinguished by the following criteria: particulate fluidization, 0.017~0.038 m/s; ABF, 0.038~0.1 m/s; turbulent fluidization, 0.1~0.2 m/s; and fast fluidization, >0.2 m/s. However, U_c and U_{se} of the CNTs are relatively lower than that of Geldart-A particles, due to the weak interaction among the CNT agglomerates and their highly porous structure.

The particulate fluidization was not always uniform, and this depends on the gas velocity. In aggregative fluidization, the distribution of the time-averaged solids fractions also showed a stronger radial non-uniformity than Geldart-A particles. An analysis of the transient density signals indicated that the non-uniformity in the radial solids distribution is due to a high level of aggregation among agglomerates near the wall, with increasing volume fraction of the dense phase near

the wall. However, on the micro-structure scale, the gas-CNT flow is more homogeneous than Geldart-A particle fluidization, which is good for gas mixing, and led to high gas dispersion coefficients of about 10^1 m^2/s for D_a and 10^2 cm^2/s for D_r.

Acknowledgments

The authors thank Prof. Wang Dezheng for reviewing this article. This work was supported by a grant from the national "863" program (No. 2003AA302630) and the National Natural Scientific Foundation of China (NSFC, No. 20236020).

Notation

D = diameter of fluidized bed, m
D_a = axial gas dispersion coefficient, m^2/s
d_a = agglomerate diameter, m
d_b = ball probe diameter, m
d_p = particle diameter, m
D_r = radial gas dispersion coefficient, cm^2/s
G = conductance, S/cm
h = data of manometer, mmH_2O
H = height of fluidized bed, mm
H_0 = initial height of fluidized bed, mm
i_b = induced ball current, A
L = distance between conductance probes, mm
n = number density of particles, m^{-3}
Re_p = particle Reynolds number
U_c = transition velocity, m/s
U_g = superficial gas velocity, m/s
U_{mb} = minimum bubbling velocity, m/s
U_{mf} = minimum fluidization velocity, m/s
U_p = particle velocity, m/s
U_{se} = serious entrainment velocity, m/s
U_t = terminate velocity, m/s
V_b = potential of ball probe, V
V_p = potential of particle, V

Greek letters

ε = voidage
ε_{mf} = solids fraction at minimum fluidization
ε_s = solids fraction
ε_{s0} = critical solids fraction
ε_{s1}, ε_{s2} = solids fractions of dilute and dense phases
μ_f = viscosity of fluid, Pa·s
ρ_a = agglomerate density, kg/m^3
ρ_b = packing density, kg/m^3
ρ_f = fluid density, kg/m^3
ϕ = dense phase fraction
ϕ_s = sphericity
ΔH = interval between neighboring measuring taps, mm

Literature Cited

1. Jono K, Ichikawa H, Miyamoto M, Fukumori Y. A review of particulate design for pharmaceutical powders and their production by spouted bed coating. *Powder Techn.* 2000;113:269–277.
2. Wank JR, George SM, Weimer AW. Nanocoating individual cohesive boron nitride particles in a fluidized bed by ALD. *Powder Techn.* 2004;142:59–69.
3. Hong RY, Li HZ. Progress in coating ultrafine particles using chemical vapor deposition in fluidized bed reactors. *Prog Natural Sci.* 1996;6:269–276.
4. Vahlas C, Juarez F, Feurer R, Serp P, Caussat B. Fluidization, spouting, and metal-organic CVD of platinum group metals on powders. *Chem Vapor Deposition.* 2002;8:127–144.
5. Qian WZ, Wei F, Wang ZW, Liu T, Yu H, Luo GH, Xiang L, Deng XY. Production of carbon nanotubes in a packed bed and a fluidized bed. *AIChE J.* 2003;49:619–625.
6. Tasirin SM, Geldart D. The elutriation of fine and cohesive particles from gas fluidized beds. *Chem Eng Commun.* 1999;173:175–195.
7. Geldart D. Types of gas fluidization. *Powder Techn.* 1973;7:285–292.
8. Wang Y, Gu GS, Wei F, Wu J. Fluidization and agglomerate structure of SiO2 nanoparticles. *Powder Techn.* 2002;124:152–159.
9. Zhu C, Yu Q, Dave RN, Pfeffer R. Gas fluidization characteristics of nanoparticle agglomerates. *AIChE J.* 2005;51:426–439.
10. Brooks EF, Fitzgerald TJ.Aggregation and fluidization characteristics of a fibrous carbon. In:1985 Annual Meeting—American Institute of Chemical Engineers, eds. New York:AIChE; 1985:21.
11. Chaouki J, Chavarie C, Klvana D, Pajonk G. Effect of interparticle forces on the hydrodynamic behaviour of fluidized aerogels. *Powder Techn.* 1985;43:117–125.
12. Wang Z, Kwauk M, Li H. Fluidization of fine particles. *Chem Eng Sci.* 1998;53:377–395.
13. Wang Y, Wei F, Jin Y, Luo T. Agglomerate particulate fluidization and E-particles. In: Jin Y, Li NN, eds. *Proc of the Third Joint China/USA Chem Eng Conf (CUChE-3)*, 2000;12–006.
14. Pacek AW, Nienow AW. Fluidization of fine and very dense hardmetal powders. *Powder Techn.* 1990;60:145–158.
15. Yu Q, Dave RN, Zhu C, Quevedo JA, Pfeffer R. Enhanced fluidization of nanoparticles in an oscillating magnetic field. *AIChE J.* 2005; 51:1971–1979.
16. Zhu C, Liu GL, Yu Q, Pfeffer R, Dave RN, Nam CH. Sound assisted fluidization of nanoparticle agglomerates. *Powder Techn.* 2004; 141:119–123.
17. Nam CH, Pfeffer R, Dave RN, Sundaresan S. Aerated vibrofluidization of silica nanoparticles. *AIChE J.* 2004;50:1776–1785.
18. Iijima S. Helical microtubules of graphitic carbon. *Nature.* 1991;354: 56–58.
19. Wang Y, Wei F, Luo GH, Yu H, Gu GS. The large-scale production of carbon nanotubes in a nano-agglomerate fluidized-bed reactor. *Chem Phys Lett.* 2002;364:568–572.
20. Hao Y, Zhang QF, Wei F, Qian WZ, Luo GH. Agglomerated CNTs synthesized in a fluidized bed reactor: agglomerate structure and formation mechanism. *Carbon.* 2003;41:2855–2863.
21. Wei F, Lin HF, Cheng Y, Wang ZW, Jin Y. Profiles of particle velocity and solids fraction in a high-density riser. *Powder Techn.* 1998;100:183–189.
22. Pulsifer AH, Wheelock TD.Electrical resistance of gas fluidized beds. In: Davidson JF, Keairns DL, eds. *Fluid Proc of the Eng Found Conf, 2nd*, eds., London: Cambridge Univ. Press; 1978;76–80.
23. Jones AL, Wheelock TD. Electrical resistivity of fluidized carbon particles: significant parameters. In: Littman H, ed. *Chem Eng Progr Symp Ser.* New York: AIChE; 1970:157–66.
24. Cheng L, Soo SL. Charging of dust particles by impact. *J Appl Phys.* 1970;41:585–91.
25. Zhu C, Soo SL. Modified theory for electrostatic probe measurements of particle mass flows in dense gas-solid suspensions. *J Appl Phys.* 1992;72:2060.
26. Li HZ, Tong H. Multi-scale fluidization of ultrafine powders in a fast-bed-riser/conical-dipleg CFB loop. *Chem Eng Sci.* 2004;59: 1897–1904.
27. Sandler J, Shaffer MSP, Prasse T, Bauhofer W, Schulte K, Windle AH. Development of a dispersion process for carbon nanotubes in an epoxy matrix and the resulting electrical properties. *Polymer.* 1999;40:5967–5971.
28. Lin Q, Wei F, Jin Y. Transient density signal analysis and two-phase micro-structure flow in gas-solids fluidization. *Chem Eng Sci.* 2001; 56:2179–2189.
29. Li Y, Wu P.A study on axial gas mixing in a fast fluidized bed. In:Basu P, Horio M, Hasatani M, eds.*Circulating Fluidized Bed III*. Oxford: Pergamon Press; 1990:581–586.
30. Du B, Fan LS, Wei F, Warsito W. Gas and solids mixing in a turbulent fluidized bed. *AIChE J.* 2002;48:1896–1909.
31. Klinkenberg A, Krajenbrink HJ, Lauwerier HA. Diffusion in a fluid moving at uniform velocity in a tube. *Indus Eng Chem.* 1953;45: 1202–1208.

32. Loezos PN, Costamagna P, Sundaresan S. The role of contact stresses and wall friction on fluidization. *Chem Eng Sci*. 2002;57: 5123–5141.
33. Cai P. Flow regime transition in dense-phase fluidized beds, Ph.D. thesis, Tsinghua University, P. R. China, 1989.
34. Bi HT, Grace JR. Flow regime diagrams for gas-solid fluidization and upward transport. *Int J Multiphase Flow*. 1995;21:1229–1236.
35. Wang ZG. Gas mixing and hydrodynamic behavior of pilot scale turbulent fluidized bed in high velocity, Master's thesis, Tsinghua University, P. R. China, 1997.
36. Zhang MH, Qian Z, Yu H, Wei F. The solid flow structure in a circulating fluidized bed riser/downer of 0.42-m diameter. *Powder Techn*. 2003;129:46–52.
37. Baerns M, Fetting F, Schugerl K. Communications on fluidized beds. V. Radial and axial gas mixing in fluidized beds. *Chem Ing Tech*. 1963;35:609.
38. Yang WQ, Liu S. Role of tomography in gas/solids flow measurement. *Flow Measurement Instrumentation*. 2000;11:237.
39. Wei F, Lu FB, Jin Y, Yu ZQ. Study on the behavior of gas mixing in gas-solid fluidized bed with composite distributor. *Shiyou Huagong (in Chinese)*. 1994;23:631.

Manuscript received Sept. 11, 2005, revision received Jun. 15, 2006, and final revision received Sept. 22, 2006.